A&A, 699, A343 (2025)
https://doi.org/10.1051/0004-6361/202555...
Astronomy & Astrophysics

We looked at the shape of 340 000 galaxies to see how it evolved through cosmic time

~~DAWN JWST Archive: Morphology from profile fitting of over 340 000 galaxies in major JWST fields~~

~~Morphology evolution with redshift and galaxy type~~

Aurélien Genin[1,2,3,⋆], Marko Shuntov[1,2,5,⋆], Gabe Brammer[1,2], Natalie Allen[1,2], Kei Ito[1,4], Georgios Magdis[1,2,4], Jasleen Matharu[1,2], Pascal A. Oesch[1,2,5], Sune Toft[1,2], and Francesco Valentino[1,4]

[1] Cosmic Dawn Center (DAWN), Denmark
[2] Niels Bohr Institute, University of Copenhagen, Jagtvej 128, 2200 Copenhagen, Denmark
[3] Ecole Polytechnique, Institut Polytechnique de Paris, Route de Saclay, 91120 Palaiseau, France
[4] DTU Space, Technical University of Denmark, Elektrovej, Building 328, 2800 Kgs. Lyngby, Denmark
[5] University of Geneva, 24 rue du Général-Dufour, 1211 Genève 4, Switzerland

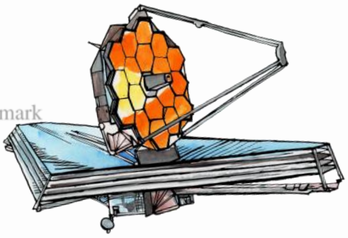

Received 13 May 2025 / Accepted 28 May 2025

SUMMARY

ABSTRACT

Using public images from the James Webb Space Telescope (JWST), we looked at 340 000 galaxies very very far in the Universe to measure their shape. The goal is to understand why and how some galaxies stop producing new stars.
We have confirmed some results that galaxies go extinctint (scientists talk of "quenching") when they are more compact. We also showed how the center of dying galaxies tend to grow faster than their outskirts.
All this work is an addition to a large database for astrophysicists about galaxies in the early Universe observed by the JWST.

Key words. techniques: image processing – catalogs – galaxies: evolution – galaxies: structure

1. Introduction — WHAT'S THE POINT?

By looking at the sky, we know that galaxies exist in different shapes.

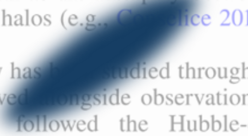

Previous astrophysicists invented ways to measure these different shapes using numbers. The goal is to more accurately see how the shape of galaxies evolved with time.

One number very often used is the Sersic index. It's small (around 1) for spiral galaxies, and larger (4 and more) for elliptical galaxies.

⋆ Corresponding authors: aurelien.genin@polytechnique.org; marko.shu...ku.dk

studies of galaxy structure, revealing, for instance, that the size distribution at fixed luminosity follows a log-normal form at $z \lesssim 0.3$ (Shen et al. 2003). The Galaxy Zoo project leveraged SDSS imaging to produce visual classifications for hundreds of thousands of galaxies (Lintott et al. 2008), enabling studies of morphological diversity and its connection to environment and star formation (e.g., Schawinski et al. 2014). At intermediate redshifts, the *Hubble* Space Telescope (HST) played a transformative role through legacy programs such as GEMS (Rix et al. 2004), COSMOS (Koekemoer et al. 2007), and CANDELS (Grogin et al. 2011; Koekemoer et al. 2011), which enabled high-resolution imaging and morphological measurements out to $z \sim 3$. These datasets allowed for extensive morphological analy[illegible] more compact, spheroidal, and concentrated than star-forming galaxies a[illegible] 2007; Barro et al. 2013, 2017; Schreiber et al. 2016), and that they undergo size growth primarily via dry mergers (e.g., van der Wel et a[illegible]ker et al. 2017). However, the mechanisms that drive galaxy quenching remai[illegible]nsformation and the cessation of star formation are causally linked, or whether they occur independently as consequences of other processes (e.g., Tacchella et al. 2015). Disentangling this connection requires large, statistically robust samples of galaxies with reliable morphological measurements spanning a wide redshift range, in order to trace structural evolution across cosmic time. Furthermore, at higher redshifts ($z \gtrsim 3$), HST imaging becomes limited to the rest-frame ultraviolet, which predominantly traces young stellar populations and can bias morphological interpretations [illegible] the groundwork for the construction of large morphological catalogs (e.g., [illegible] Kawinwanichakij et al. 2021), providing critical insights into the growth and structural transformation of galaxies over more than 10 billion years of c[illegible]

To look at galaxies and how they evolve with time, telescopes have to look very far in the Universe (remember, the further we observe, the more we go back in time).

Many telescopes have done that, such as Hubble and now the JWST. This gives a very large set of observations, with the JWST pushing even further than Hubble!

The James Webb Space Telescope (JWST) has opened a new era in the study of galaxy morphology, enabling rest-frame optical measurements out to $z \gtrsim 7$ with unprecedented depth and resolution. Studies based on JWST observations have revealed the evolution of galaxy morphology and size for both star-forming and quiescent galaxies out to unprecedented redshifts (e.g., [illegible]n et al. 2025; Matharu et al. 2024; Wright et al. 2024; Ito et al. 2024; Yang et al. [illegible] galaxies rem[illegible]aller effective radii and higher Sérsic indices, even at early times. Neverthe[illegible]date have focused on specific galaxy selections, such as mass- or color-selected subsamples, or have been limited to individual fields. As a result, there is no consistent, flux-limited morphological catalog across different major JWST fields and redshifts. This limit[illegible]studies of galaxy structure, particularly for rarer populations such as quiesc[illegible]T.

Astronomers have preferred regions in the sky that they observe with different telescopes. This allows to compare their measurements and better understand the Universe. The ones we used are called: EGS, GOODS, COSMOS, UDS (Ultra Deep Survey!).

In this work, we build one of the largest and most uniform morphological catalogs to date using JWST imaging, enabling consistent structural measurements across multiple fields and redshifts. We utilize publicly available mosaics from the DAWN JWST Archive (DJA, Valentino et al. 2023), which compiles deep NIRCam imaging from major extragalactic surveys, including CEERS, PRIMER (UDS and COSMOS), and GOODS. These are accompanied by matched photometric redshifts and physical parameters. To measure galaxy morphology, we carry out two-dimensional surface brightness profile fitting using SourceXtractor++ (Bertin et al. 2020; Kümmel et al. 2020), a modern, scalable tool optimized for catalog-level model fitting in large multiband datasets. We fit each galaxy with both a single-component Sérsic profile (Sérsic 1963) and a two-component Bulge+Disk (B+D) model consisting of an exponential disk ($n_S = 1$) and a de Vaucouleurs bulge ($n_S = 4$). This dual-model approach allows us to probe structural diversity more flexibly and to derive key parameters, such as the Sérsic index (n_S), the effective radius, the axis ratio, and the bulge-to-total ratio (B/T). We apply this modeling to all sources above a flux an[illegible]ho-logical catalog spanning approximately 340 000 sources across [illegible]nity to carry out detailed statistical studies of galaxy morphology evolution throughout cosmic time.

We set out to measure the shape of A LOT MORE galaxies by looking at all these large and deep regions of the sky at once.

Thi[illegible]nt spread function (PSF) reconstruction are presented in Section 2. In Section 3, we describe our method for measuring the morphology and sizes of galaxies across such a large field. In Section 4, we present our results on the correlation between morphology and the UVJ diagram, as well as the size evolution in the Sérsic and B+D models. We summarize our results in Section 5. We adopt a Planck Collaboration VI (2020) ΛCDM cosmology with $H_0 = 67.4\,\mathrm{km\,s^{-1}\,Mpc^{-1}}$, $\Omega_{m,0} = 0.315$. All magnitudes are expressed in the AB system (Oke 1974).

WHAT DATA DID WE USE?

This work uses NIRCam images (Rieke et al. 2005) from public surveys of the JWST, processed as part of the DAWN JWST Archive (DJA), mosaic release v7. [illegible]ne repository [illegible]s, and spectroscopic data from public JWST data, and [illegible] described in more [illegible] 2025). In this work, we carry out morphological measurements in several major extragala[illegible] covering a total area of ~500 arcmin^2. We focus on the following fields:

Because we use public images, taken by other astronomers using the JWST, it's always a good thing to mention them.

1. EGS from CEERS (DD-ERS 1345 Finkelstein et al. 2023);
2. GOODS from JADES (GTO 1180, 1181, 1210, 1287 Eisenstein et al. 2023);
3. UDS from PRIMER UDS (GO 1837 Donnan et al. 2024);
4. COSMOS from PRIMER COSMOS (GO 1837 Donnan et al. 2024).

Table 1 presents the area and photometric bands used in these fields and their 5σ depths (computed from empty apertures by Weibel et al. 2024).

2.1. Images

The images used in this work are drawn from the DJA [illegible] the whole [illegible] gds-grizli-v7.2, gdn-grizli-v7.3, primer-uds-north-grizli[illegible]rimer-cosmos-west-grizli-v7.0, and primer-cosmos-east-grizli-v7.0.

The [illegible] photometric units (10 nJy), which we used to run SourceXtractor++, alongside the [illegible]hat provide the inverse variance distribution. For source detection, we used the inverse-variance weighted stack of the long-wavelength filters (specified with `ir` in place of the filter in the image name). We did not

The images have also already been processed by the Cosmic DAWN Center (where I was doing my internship that led me to do this work) to be ready to be used by scientists.

Table 1. Summary of the fields covered in this work.

Field	Area (arcmin^2)	Depth (mag)	Bands
EGS	82.0	29.16	F115W, F150W, F182M, F200W, F210M, F277W, F356W, F410M, F444W
GOODS	67.3	29.93	F090W, F115W, F150W, F200W, F277W, F356W, F444W
PRIMER-UDS	224.4	28.51	F090W, F115W, F150W, F200W, F277W, F356W, F444W
PRIMER-COSMOS	127.1	28.62	F090W, F115W, F150W, F200W, F277W, F356W, F444W

Notes. All images are from the DJA and were processed prior to this work. The survey areas and 5σ depths computed from empty apertures correspond to the F277W band and were calculated by Weibel et al. (2024).

apply any PSF convolution, since SourceXtractor++ convolves the source models with the corresponding filter PSF (see Sect. 2.3).

2.2. Catalogs

The DJA also provides photometric and photo-z catalogs produced with SExtractor (Bertin & Arnouts 1996) and EAZY ([illegible]) [illegible] catalogs as our principal list of sources [illegible] field. Although we performed a separate detection with SourceXtractor++ ([illegible]) [illegible] model-fitting-based measurements for the same sources. This appr[illegible] and physical parameters from spectral energy distribution (SED) fittings with EAZY [illegible] catalogs. In this work, we used the EAZY output to investigate morphology evolution as a function of redshift and galaxy type (Sect. 4).

We also used measurements done by astrophysicists at DAWN of other properties of these galaxies: their distance, their mass, their color, their brightness...

2.3. Point spread function reconstruction

Accurate model fitting requires precise characterization of the instrument's PSF. The PSF results from light diffraction at the aperture of the telescope and defines the resolution limit of JWST. We empirically modeled the PSF from the final mosaics using PSFEx ([illegible] 2011), which builds a model for the PSF by fitting [illegible] provided in an input catalog. Recent work by Berman et al. (2024) shows that PS[illegible]

To select point sources, we developed a method inspired by [illegible] (2007). This method uses the MU_MAX and MAG_AUTO measurements from SExtractor. The parameter MU_MAX represents the surface brightness of the brightest pixel of a source, [illegible]-like elliptical aperture magnitude. In the MU_MAX/MAG_AUTO plane (shown in Fig. 1), the point-like sources follow a line of slope equal to one (referred to in this paper as the "starline"), and extended sources form a distinctive cloud above it. We added thresholds for MAG_AUTO: a minimal value to avoid selecting saturated

Every telescope (just like the camera in your phone) takes pictures that are somewhat blurry. We need to measure this blurriness to correct for it when we'll measure the shape of galaxies.

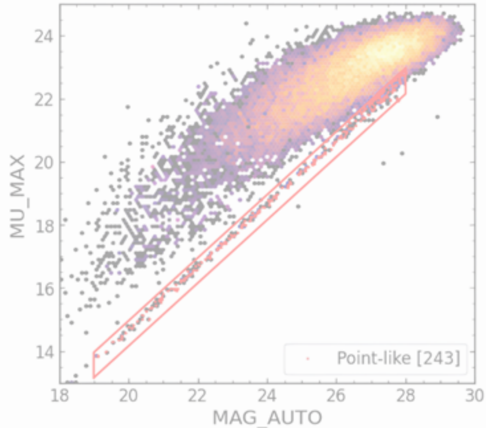

Fig. 1. Point-like sources selection for PSF estimation. The plot shows the distribution (log scale) of sources from the GOODS-S field (F200W) in the MU_MAX/MAG_AUTO plane. The red box shows the starline [illegible] red dots.

This is done by looking at stars (in the Milky Way, our galaxy) and what they look like. With the JWST, they look something like that!

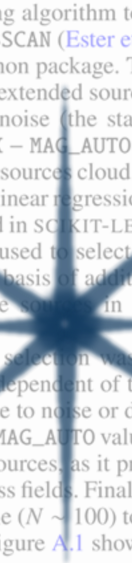

so[illegible] maximal value to avoid including sources in the extended sources cloud.

Detecti[illegible] linear regression. However, to avoid bias from the extended sources cloud, we first applied a clustering algorithm to detect this point cloud and remove it. We used DBSCAN (Ester et al. 1996), implemented in the SCIKIT-LEARN Python package. This algorithm identifies cores of high density (the extended sources cloud) while excluding points considered as noise (the starline). We then applied a threshold on the MU_MAX – MAG_AUTO value to further remove outliers from the extended sources cloud. Finally, we detected the starline using the RANSAC linear regression algorithm (Fischler & Bolles 1981), implemented in SCIKIT-LEARN. The threshold and width around the starline used to select point-like sources were chosen empirically on the basis of additional tests. Fig. 1 shows the selection of point-like sources in the MU_MAX/MAG_AUTO plane.

The point-like source selection was expected to physically yield the same sample, independent of the band used. However, slight differences arose due to noise or differences in the threshold used for the MU_MAX – MAG_AUTO value. We chose the F200W band to select point-like sources, as it provided the most consistent starline detection across fields. Finally, we visually inspected a randomly selected sample ($N \sim 100$) to verify that the selected sources were point-like. Figure A.1 shows examples of the PSFs in the GOODS-S field.

OUR MEASUREMENTS

3. Morphological measurements

3.1. SourceXtractor++

In [illegible] galaxy morphologies measured from JWST images. To accomplish this, we used SourceXtractor++ (hereafter abbreviated as SE++; Be[illegible] 2020; Kümmel et al. 2020), the successor of the classic SExtractor Bertin & Arnouts (1996), which performs brightn[illegible] multiband images. The principal advantage of SE++ is that it is optimized exactly for the purpose of large catalog creation – it can simultaneously fit all sources in arbitrarily large mosaics and

We didn't start from scratch. We used a tool called SourceXtractor++ (the successor to SEXtractor, yes that's its real name) that can measure the shape of galaxies with a given model (like the Sérsic index).

in different bands, without the need for prior sample selection, cutout creation, and masking. Additionally, its flexible model fitting allows the user to define any model using a simple Python configuration file. In the following, we describe our models and catalog-makin[illegible]

In our work, we used two models of shape for galaxies.

3.2. Brightness profile models

To measure galaxy morphology, we modeled the brightness profi[illegible] provides full control over the model. To maximize scientific applications, we [illegible]

The first one is the Sersic model. It looks at galaxies as blobs of light and measure their shape by how sharp their edge is.

1. The Sérsic model (Sérsic 1963), parameterized by a single shape parameter, the Sérsic index n_S; the effective radius R_e; the axis ra[illegible] and the total flux f_{tot}. In this work, we fit for the two components of the ellipticity, e_1 and e_2, which are directly linked to (a/b) and θ. The priors [illegible] for these parameters are presented in [illegible].
2. [illegible] Disk (B+D[illegible], a composite o[illegible] [illegible]disk ($n_S = 1$) and a de [illegible] bulge ([illegible] Sérsic profile. It is parametrized by the effective radii [illegible] disk, R_{disk}, and bulge, R_{bulge}; the axis ratios $(a/b)_D$ and $(a/b)_B$; a common angle θ_{BD}; the total flux of both components, $f_{BD,tot}$, and the bulge-to-total ratio $B/T = f_{B,tot}/f_{BD,tot}$. The B/T prior is a bell curve ranging from 5×10^{-5} to 1, with a mean and spread that increase as a function of wavelength.

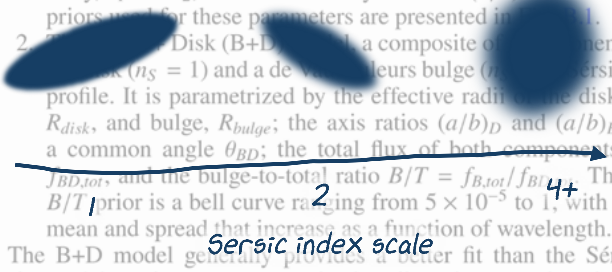

The B+D model generally provides a better fit than the Sérsic model, as it more accurately describes the central region of galaxies, particularly the presence of a bulge or a dimmer center compared to a Sérsic profile. However, because it has more parameters, it is more computationally intensive and can, in some cases, lead to degeneracy in the model parameters, especially for fa[illegible] may not be distinguishable.

The SE++ tool performs model fitting simultaneously on multiple images, t[illegible]ds. In this work, we constrain the morphological parameters (R_{eff}, n_S, (a/b), and θ) to b[illegible] approach yields final values that represent a weighted average over the entire wa[illegible]. The SE++ configura[illegible] GitHub[1].

The second model is called Bulge+Disk. It's the superposition of two Sersic model:
- One of index 4 for the core (the bulge) of the galaxy
- One of index 1 for the outskirt (the disk) of the galaxy

3.3. Tiling

It is theoretically possible to run SourceXtractor++ directly on the [illegible] and computing power limitations, we chose to tile the full images. This a[illegible] paral- lelization. We divided the mosaics into $2' \times 2'$ tiles, with $0.5'$ overlap, to [illegible] were fully present i[illegible]

This B+D model better describes some galaxies that have a very bright core (because of a supermassive black hole for example).

3.3.1. Catalog merging

To merge the sub-catalogs, we iterated over each tile to append them and create a catalog covering the whole field. At each iteration step, we cross-matched with the previously appended sub-catalogs and discarded the matched duplicates from the overlap regions. For sources that are matched (in the overlap region), we chose the one with the smallest uncertainty in the F200W magnitude, as measured by SourceXtractor++. As the model fitting was performed independently for the Sérsic and B+D models, this step was performed separately to produce one catalog per model. The F200W band was chosen because it has better resolution compared to the LW channel, and galaxies are generally brighter in it than in other bands of the SW channel.

Finally, we cross-matched the two model-fitting catalogs with the DJA catalogs. This step allowed us to remove false detections (which were frequent near the edges of images), retain the same list of sources, and provide additional morphological measurements to the DJA catalogs. We chose a threshold of 0.3″ as the cutting distance to validate a match. This threshold was set manually using the histogram of angular distances produced by the cross-match. This value corresponded to 5 pixels in the LW channel and 10 pixels in the SW channel of NIRCam, which was acceptable and could be the result of differences between the source centroids estimated in SExtractor and SourceXtractor++.

3.3.2. Merging of the model and residual images

The SE++ tool produces model and residual images. We merged only the model sub-images and generated a mosaic residual image afterward. To merge the sub-images, we used the `reproject_and_coadd` function from the `reproject` Python package (Robitaille 2018), which reprojected and co-added the images on a frame specified by the World Coordinate System (WCS) of the native DJA images. This ensured that the merged full model images had the same pixel scale, center, and orientation as the DJA images. We used this to generate mosaic residual images by subtracting the mosaic model images from the source DJA images.

3.4. Flagging and completeness

As mentioned previously, our aim was to add morphological measurements to the DJA catalogs. Therefore, by cross-matching, we retained the same number of rows (sources) in our catalogs as in the DJA catalogs. Furthermore, we added a `flag` keyword with four possible values as follows:

0 : the source was not fitted (no morphological data).
1 : a potential artifact occurred during model fitting.
2 : fitting was performed successfully. This value gives science-ready data.
3 : the source has S/N < 3 or a magnitude fainter than the 5σ depth of its corresponding survey. The S/N was computed by SourceXtractor++ on the detection image.

The distribution of the `flag` values is shown in Fig. 2. Seventy to eighty percent of the sources were successfully fitted (`flag=2`). This indicates that the SourceXtractor++ minimization algorithm converged and the parameter values were no[illegible] max- imum of the allowed range. Sources without morphological d[illegible] + detection step and are likely artifacts or faint sources near the ima[illegible]. Poten- tial a[illegible] with some parameters remaining at their initial values or that strayed to the ext[illegible]. Typically, this indicates a poor fit; therefore, we flagged such sources. For the Sérsic model, this includes sources with $(a/b) > 0.99$, $|n_S - 0.36| < 10^{-4}$, $n_S > 8.35$, or $n_S < 0.301$. For the B+D model, this includes $(a/b)_D > 0.9999$, $(a/b)_D < 0.10001$, or $|(a/b)_D - 0.5| < 10^{-5}$. These values were chosen manually by identifying artifacts in the parameter distribution and by visual

To run SourceXtractor++ on all our images, we have to slice them in small patches. This is simply to not hurt too much the computers that will have to do measurements.

[1] https://github.com/AstroAure/DJA-SEpp/blob/main/config/sepp-config.py

Table 2. Completeness of the morphology measurements using SourceXtractor++.

Field	DJA	Sérsic	Bulge+Disk	Both
CEERS	67 035	52 604 (78.5%)	59 046 (88.1%)	**51 329 (76.6%)**
GOODS-S	57 355	44 931 (78.3%)	52 754 (92.0%)	**44 016 (76.7%)**
GOODS-N	65 481	53 291 (81.4%)	58 852 (89.9%)	**51 465 (78.6%)**
PRIMER-UDS (N)	68 857	58 947 (85.6%)	67 134 (97.5%)	**57 945 (84.2%)**
PRIMER-UDS (S)	65 864	57 397 (87.1%)	64 537 (98.0%)	**56 476 (85.7%)**
PRIMER-COSMOS (E)	50 655	42 359 (83.6%)	48 496 (95.7%)	**41 597 (82.1%)**
PRIMER-COSMOS (W)	51 362	40 493 (78.8%)	46 964 (91.4%)	**39 704 (77.3%)**
Total	426 609	350 022 (82.0%)	397 783 (93.2%)	**342 892 (80.4%)**

Notes. Values in the table show only sources with F277W magnitudes below the 5σ depth of each field, and a S/N >3. For the SourceXtrac-tor++ columns, the values correspond to sources successfully fitted (flag=2); see Sect. [illegible] the DJA catalogs with the same magnitude and S/N cut.

All the galaxies that have been correctly measured: 340 000 galaxies!

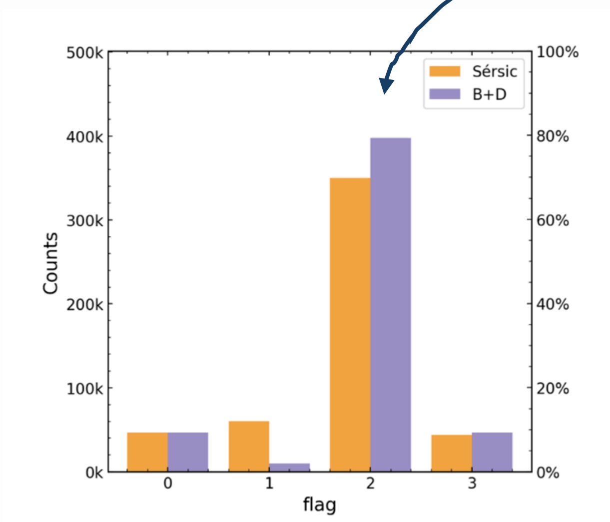

Fig. 2. Histogram of the flag values for the full catalogs. The percentages are relative to the total number of sources in the DJA catalogs. Two distinctive histograms for the Sérsic and Bulge+Disk models are shown bec[illegible] major-ity (70–80%) of sources are correctly fitted and provides science-ready m[illegible] inspection. These sources should be handled with care by the user.

For some mysterious reasons, the program sometimes fails to measure the shape of a galaxy. We identify these failures, and mark the one that have correctly been measured. This way, we know that we have been able to measure the shape of 80% of the galaxies in the images!

Since the list of detected and measured sources by SourceXtractor++ is slightly different from the initial DJA list, w[illegible] cata-logs. Table 2 presents the number of galaxies in each field used in th[illegible] (flag=2) in each model (Sérsic and B+D) from our work.

The completeness was measured relative to the number of galaxies in the DJA catalogs, using the same quality cut on S/N and magnitude as S/N >3 and mag $<5\sigma$ depth (flag=3) on both. In total, our catalog consists of 342 892 sources with reliable model fitting and science-ready, making it one of the largest morphological catalogs based on JWST observations.

A total of 80.4% of the DJA S/N >3 and mag $<5\sigma$ depth sources were successfully fitted with both a Sérsic and a B+D model. The completeness is higher for the B+D model than for the Sérsic model. This is likely because the B+D model is a better description for some sources whose Sérsic model parameters tend toward the minimum or maximum allowed values (therefore classified as flag=1). Finally, we analyzed the distribution of certain physical parameters (F277W magnitude, $z_{\rm phot}$, mass, and Kron radius) for the non-detected sources (flag=0) and potential artifacts (flag=1). We did not find any significant correlation between these parameters, indicating that the incompleteness due to flag=1 is not biased with magnitude, redshift or stellar mass.

Therefore, we consider our morphological catalogs to have a relatively high completeness compared to the DJA, and, as such, they provide highly valuable information for studying the morphology of galaxies and its evolution through cosmic time, as demonstrated in Sect. 4.

3.5. Comparisons with previous work

To validate our measurements, we compared them with previous morphological catalogs in the same fields, particularly van der Wel et al. (2012). These catalogs contain Sérsic modeling performed using *Hubble* Space Telescope (HST) observations in the same fields used in this work: GOODS, EGS, UDS, COSMOS. By cross-matching them with our catalog and selecting only early-type galaxies (see Eq. (2)), we find 3263 matches with S/N >10.

The size and morphology of galaxies are known to differ in different wavelength ranges. To ensure that we compared morphologies measured at similar observer-frame wavelengths, we used the measurements in F160W from van der Wel et al. (2012). However, since our measurements correspond to the averaged morphology over NIRCam's wavelength range (~1–5 µm), we scaled the effective radii $R_{\rm eff}$ in van der Wel et al. (2012) to 2.5 µm using the following scaling relation:

$$\frac{\Delta \log R_{\rm eff}}{\Delta \log \lambda} \ldots \quad (1)$$

To make sure that our measurements are reliable, we compare some of them with previous studies that used different tools.

w[illegible] wavelength dependence of $R_{\rm eff}$ for [illegible] galaxies. We note that a more complex version of this relation has been proposed by the same authors, which integrates the effect of redshift and stellar mass. However, we adopted this simpler and more general relation for comparison purposes.

Figure 3 shows the one-to-one comparisons between the two works for $R_{\rm eff}$ (top middle panel) and the Sérsic index $n_{\rm S}$ (top

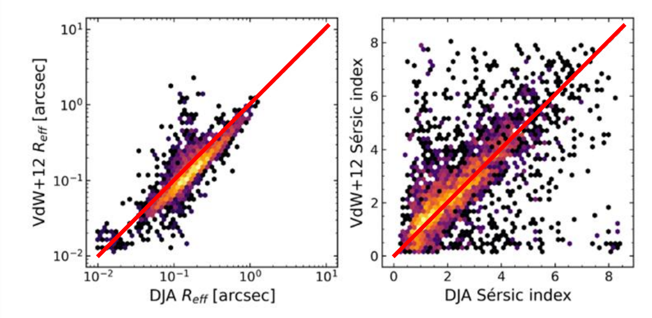

Fig. 3. Comparison between Sérsic model fitting in our work and van de[illegible] compares e[illegible]ctive radii R_{eff} and Sérsic index n. We corrected the R_{eff} valu[illegible] um, to 2.5 µm using Eq. ([illegible]), in order to match the average wavelength of our J[illegible] cell in log scale. Gray dotted lines show identical values between the tw[illegible] right pane[illegible] and the axis ratio (a/b) (bottom panels). In general, there is good agreement in the effec[illegible]r radii from our measurements. One reason for the slight offset could be the scaling using Eq. (1) that we applied. Without this scaling, the trend inverses and our effective radii are smaller than those of van der Wel et al. (2012).

Ideally, all the points would be on the red diagonal line. But because we used different images and tools, it's normal that there's some dispersion. However, they pretty much follow the correct trend. So our measurements are good!

WHAT CAN WE LEARN FROM ALL THIS?

4. Morphological evolution with redshift and galaxy type

To demonstrate the scientific application of our morphological catalogs, we investigated statistical distributions of several morphology indicators as a function of redshift and galaxy type. Our measurements cover a wide range of redshifts, enabling studies of m[illegible] we used the photo-z, rest-frame colors, and other physical parameters from the DJA E[illegible] catalogs. In particular, we investigated morphological evolution as a function of galaxy [illegible] vs. star-forming).

The main motivation for this work was to look at the difference in shapes between galaxies that form new stars and « dead » galaxies (so called quiescent galaxies)

4.1. [illegible]

To [illegible] and redshift, we used the UVJ color diagram to select star-forming and quiescent galaxies ([illegible]). In principle, the UVJ selection criteria for quiescent galaxies change with redshift (Williams et al. 2009). However, for our qua[illegible] analysis, we adopted a redshift-independent selection corresponding to the $0.7 < z < 1.3$ range used in Schreiber et al. (2016), who also investigated the morphology dependence of the UVJ diagram from HST observations:

To separate star-forming from dead galaxies, we can look at their color. Young stars are generally blue because they are hotter, whereas old stars are red because they are cooler. (Yes, this is the opposite from the colors on your faucet...)

Because of this, we know that dead galaxies are redder than star-forming ones. We can therefore look at the shape of the galaxies and compare them to their color!

$$UVJ_{\rm quiescent} = \begin{cases} V - J < 1.6, \text{ and} \\ U - V > 0.88(V - J) + 0.49. \end{cases} \quad (2)$$

In addition, we focused our analysis on $\log M_\star/M_\odot > 10$, `flag=2`, and S/N >10, resulting in 13 685 galaxies. This ensured that our sample had sufficiently high S/N and robust morphological estimates from the model fitting.

First, we investigate the location of galaxies in the UVJ diagram as a function of the Sérsic index, n_S, and redshift. Fig. 4 shows the UVJ diagram in six redshift bins at $0 < z < 6$ (in different panels), color coded by the Sérsic index. The dotted lines mark the regions separating star-forming and quiescent galaxies (Eq. (2)). Fig. 4 shows a clear correlation between the Sérsic index and UVJ colors. There is a gradient of the Sérsic index, n_S, in a direction roughly orthogonal to the boundary between quiescent and star-forming galaxies, such that galaxies with a higher Sérsic index preferentially populate the redder and quiescent UVJ region. This trend holds for the different redshift bins. For $z > 4$, the samples are too small to draw statistically robust conclusions, especially for quiescent galaxies.

Second, because we also used B+D models to fit the galaxies in our catalogs, we could analyze how their B/T values populate the UVJ diagram. For this analysis, we used the B/T measured in the F200W band because it offers better resolution, being in the SW channel. Figure 5 shows UVJ diagrams for three broad redshift ranges and three B/T ranges. The color indicates the B/T value, with the color scale indicated at the top. We also show the contours estimated by kernel density. Fig. 5 shows that bulge-dominated galaxies ($B/T > 0.6$) preferentially occupy the quiescent region, whereas disk-dominated galaxies ($B/T < 0.2$) occupy the star-forming region. Intermediate galaxies that show both bulges and disks ($0.2 < B/T < 0.6$) form a diverse population that can be classified as both star-forming and quiescent based on their UVJ colors. However, there is a trend showing that galaxies with a higher B/T preferentially occupy the quiescent UVJ region. At $z > 3$ there are more galaxies with higher B/T that are star-forming than quiescent. This results from the relative rarity of quiescent galaxies at these epochs, as well as from the presence of a population of compact star-forming galaxies (e.g., blue nuggets, Barro et al. 2013; Dekel & Burkert 2014, which we discuss further in the next part of this section). These qualitative trends from the independently fitted B+D model are in good agreement with those from the [illegible] of the morphological measurements.

To further investiga[illegible] the correlation between bulge- and disk-dominat[illegible]ed morphology and star formation activity, we defined two classes based on the two independent morphology estimates, n_S and B/T, as follows:

1. Bulge-dominated galaxies: $n_S > 1$ and $B/T > 0.5$.
2. Disk-dominated galaxies: $n_S < 4$ and $B/T < 0.5$.

With this, we attempted to provide a robust binary classification of whether a galaxy is disk- or bulge-dominated and explore how [illegible]

In Fig. 6, we show the UVJ diagrams in the same redshift ran[illegible]ges as in Fig. 4, with color indicating the two different classes: red for bulge-dominated galaxies and blue for disk-dominated galaxies. We plotted kernel density contour lines for each class. This classification is consistent with the broad conclusion that quiescent galaxies are bulge-dominated and star-forming galaxies are disk-dominated.

The disk-dominated sample still exhibits a degree of bimodality, with a small population of quiescent galaxies. [illegible] while star formation is typically associated with disk galaxies, quiescent disks do exist. At lower masses, quenching is often environmentally driven, particularly via strangulation (Larson et al. 1980; Moran et al. 2007), ram pressure stripping (Gunn & Gott 1972), and galaxy harassment (Moore et al. 1996, 1998) in dense environments (Peng et al. 2010; Cortese et al. 2021). At higher masses, some fast-rotating quiescent disks can

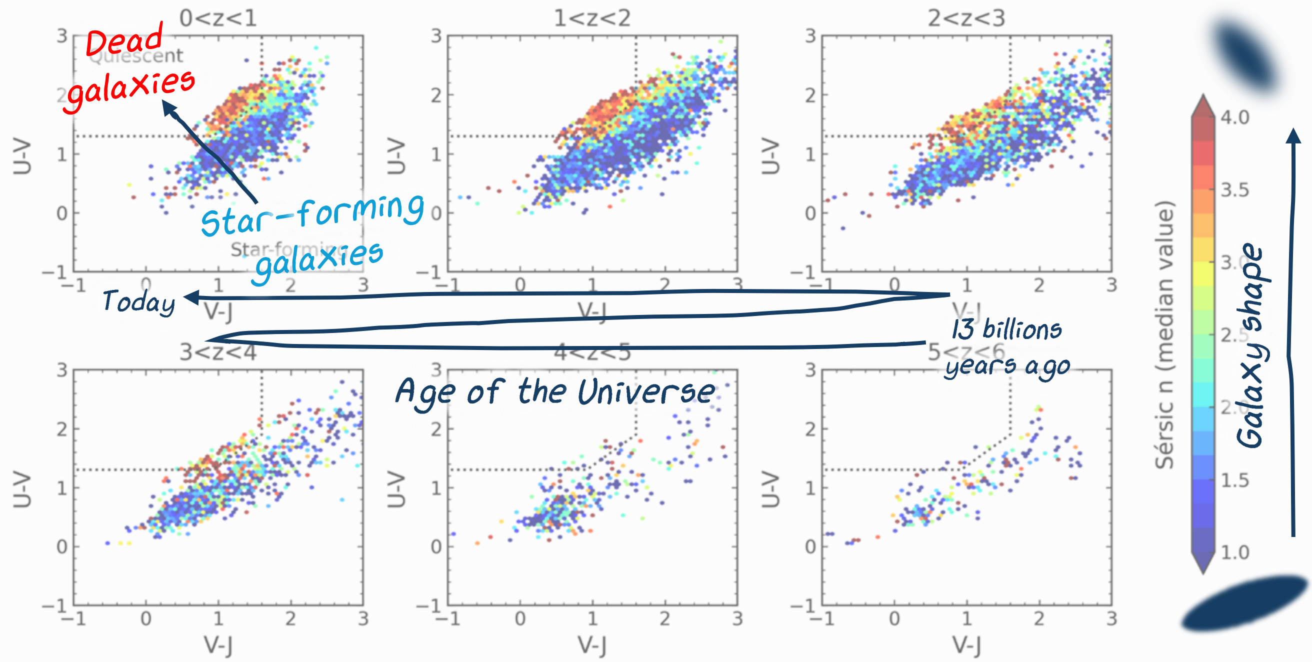

Fig. 4. Distribution of Sérsic indices, n_S, in the UVJ color space for different redshift ranges, for galaxies with $\log M_\star/M_\odot > 10$. The color of each hexagonal bin represents the median value of n_S, as indicated by the colorbar. The dotted line shows the quiescent vs. star-forming separation using Eq. (2). The quiescent region is predominantly populated by galaxies with high Sérsic indices ($n_S \gtrsim 3$).

The figure above shows how the shape of galaxies is linked to their color (and so whether they produce new stars or not)

We see that dead galaxies always have a high Sersic index, whereas star-forming galaxies have a low Sersic index.

This confirms that star-forming galaxies are generally disk galaxies and dead galaxies are elliptical.

Moreover, we see that this conclusion holds even at different epochs (although there are fewer dead galaxies in the early Universe because they haven't had the time to go extinctint).

form through a combination of mild dissipative contraction and secular evolution (Toft et al. 2017; D'Eugenio et al. 2024). These quiescent disks may also result from gas exhaustion following a compaction event or mergers that preserve disk kinematics bu[illegible] 2015).

Bulge-dominated galaxies [illegible] occupy the quiescent UVJ region out to $z \sim 3$, with a small bimodality appearing in the star-forming region at higher redshifts. This indicates that bulge[illegible] cosmic times, but by $z < 1$, most have migrated toward quiescence. This trend may [illegible] bulg[illegible] with or precedes quenching, consistent with theoretical and observational evidence for compaction-driven quenching (e.g., Barro et al. 2013, 2014; Tacchella et al. 2015, 2016). The location of bulge-dominated galaxies in the UVJ diagram – toward bluer colors compared to the main disk-dominated population – supports a fast quenching scenario, in which lower-mass, young, star-forming galaxies undergo rapid quenching [illegible] Merlin et al. 2018; Belli et al. 2019). This is consistent with the blue nugget phase, where galaxies experience a burst of compact st[illegible] quenching into red nuggets (e.g., Dekel & Burkert 2014; Zolotov et al. 2015; Barro et al. 2017). Finally, the lower number of bulge-dominated galaxies in the higher redshift ranges is consistent with the inverted Hubble classification evolution: galaxies form as disks and evolve to bulges (e.g., Quilley & de Lapparent 2022).

This qualitative analysis of the correlation between quenching and morphology is consistent with the current picture from both theory and observations. Importantly, by providing morphological measurements from JWST for such a large sample, our work paves the way for more in-depth and quantitative population studies that can unveil the details of galaxy quenching and the accompanying morphological transformations.

4.2. Size evolution

[illegible] the evolution of the size with redshift for galaxies classified by their morphology type (namely, bulge- and disk-dominated). We analyzed the radii from the two inde[illegible] model, and the disk effective radius r_{disk} and bulge effective radius r_{bulge} [illegible] in kpc by converting the measured angular radius, using the z_{phot} given in the DJA EAZY catalogs.

In Fig. 7, we show the size evolution with z_{phot} for the Sérsic effective, disk, and bulge size measures for galaxies with $\log M_\star/M_\odot > 10$, which corresponds to a mean mass of $\approx 4 \times 10^{10}$ $M_\odot$. We show the trend for all galaxies, disk- and bulge-dominated as defined in Sect. 4.1. We note that our sizes were [illegible] size-redshift evolution studies typically use the size measured in [illegible] probes the same rest-frame optical range over the studied redshift range. This means that our measurements probe the rest-frame optical at $z \gtrsim 0.5$; however, this approach may introduce differences when comparing our results with studies that base their size measurements on a single band for a defined redshift range.

Our measurements show that the overall size (r_e, from the Sérsic model) of all galaxies with $\log M_\star/M_\odot > 10$ increases with redshift from about 1 kpc at $z \sim 5$ to ~2.5 kpc at $z \sim 0.5$. Disk-dominated galaxies show larger sizes by about 0.1–0.2 kpc compared to the whole sample, and increase with time, while

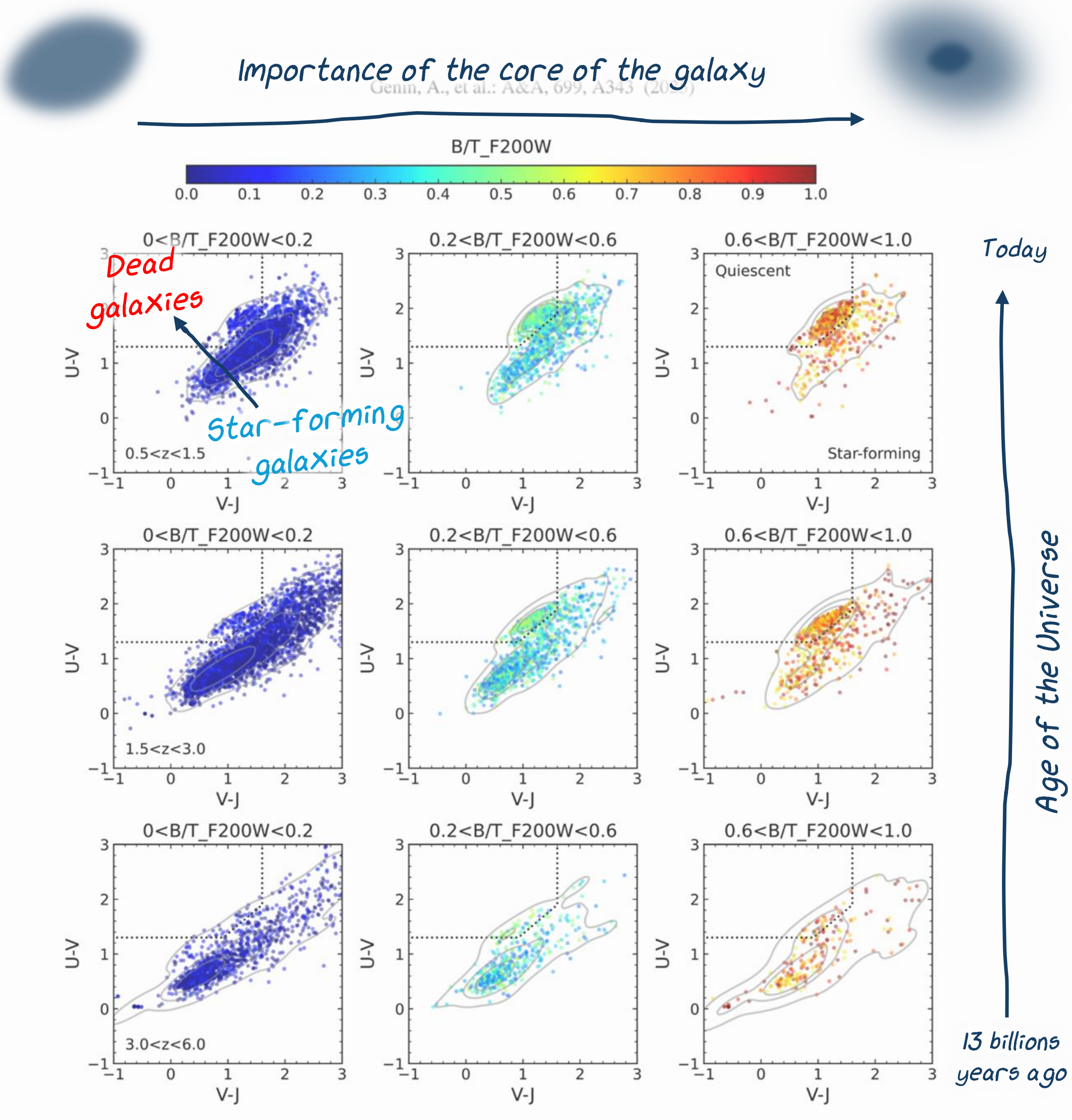

Fig. 5. Distribution of B/T in the UVJ color space for different redshift and B/T ranges, for galaxies with $\log M_\star/M_\odot > 10$. Each point is colored by its B/T value in the F200W ... The contours indicate 25, 50, and 75% of the density. Bulge-dominated galaxies (high B/T) predominantly occupy the quiescent region, whereas disk-dominated galaxies (low B/T) are generally in the star-forming region of the UVJ space.

Using the Bulge+Disk model shows a similar story:

Dead galaxies have generally a bright core and a dim disk.
Star-forming galaxies have generally a dim core and a bright disk.

But this is also correct the other way around:

Galaxies that have a bright core are generally dead.
Galaxies that have a bright disk are generally forming stars.

And we don't know yet whether one of this causes the other (is it the death of the galaxy that makes it become denser ? Or is it its compactification that makes it die ?) or if there's an external effect that causes both.

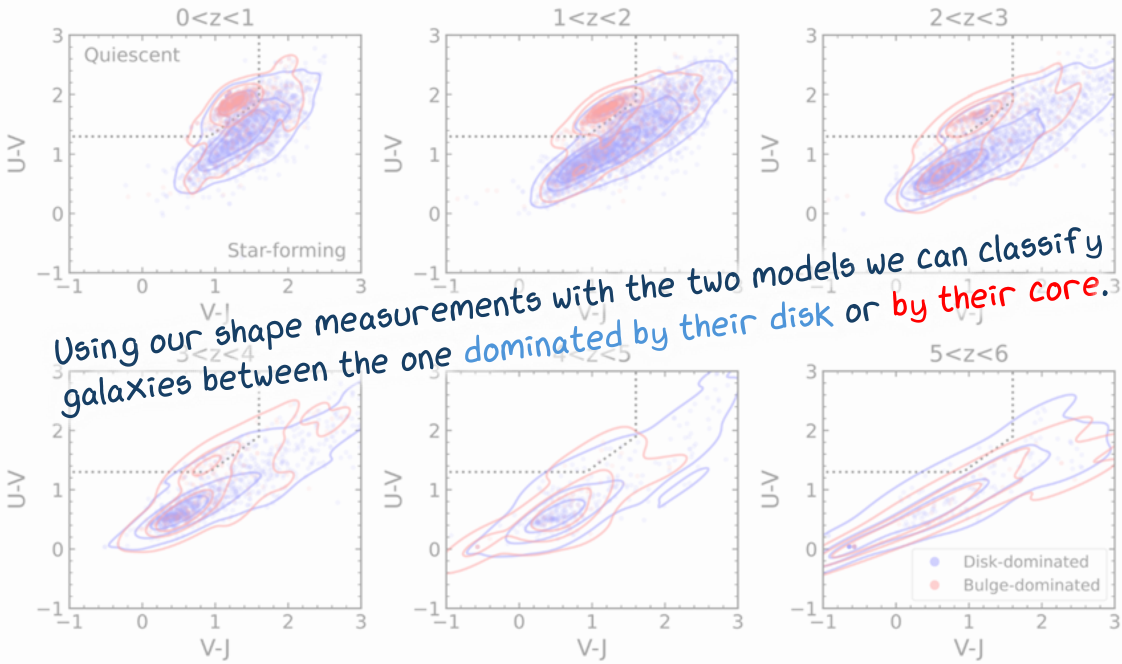

Fig. 6. UVJ color diagram for bulge- and disk-domi[nated] ... and B/T, estimated independently. Contour lines show kernel density estimates corresponding to 25, 50, and 75% of the density.

Galaxies grow with time, but dead galaxies have had a sudden jump in size whereas star-forming galaxies grew steadily.

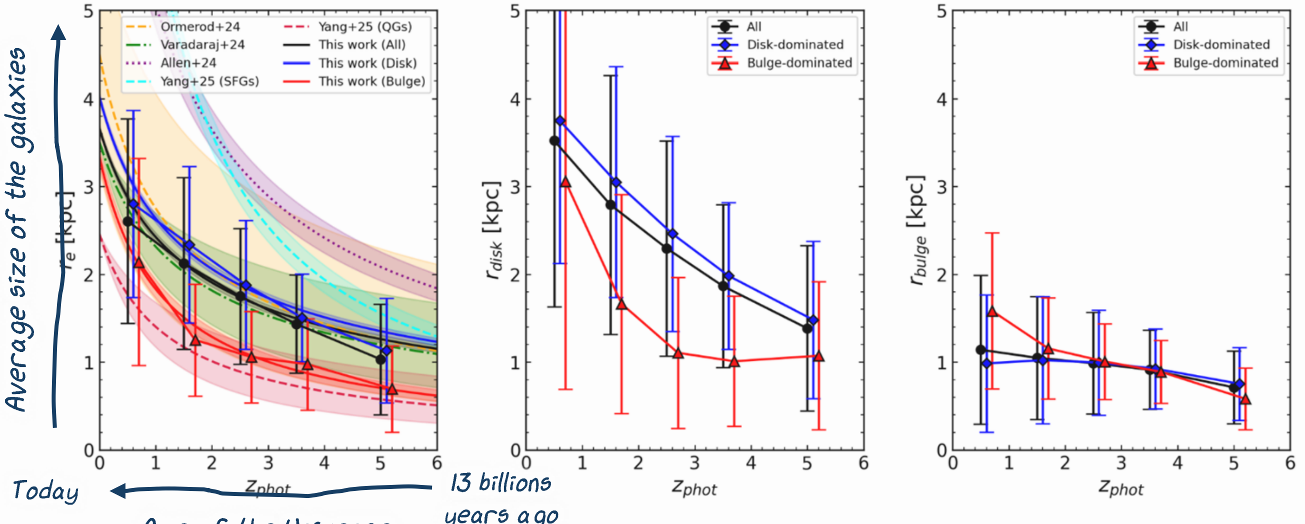

Fig. 7. Evolution of galaxy sizes as a function of redshift. The plots show the Sérsic effective radius r_e (left), the disk effective radius r_{disk} (center), and the bulge effective radius r_{bulge} (right) as a function of z_{phot} for log $M_\star/M_\odot > 10$ galaxies. This corresponds to a mean mass of $\approx 4 \times 10^{10}$ $M_\odot$. The points with error bars show the mean and 1σ at a given redshift for all galaxies (black), disk-dominated galaxies (blue), and bulge-dominated galaxies (red). The r_e evolution is modeled in the left panel for all galaxies ... following $\propto (1+z)^\alpha$ (see Sect. 4.2). We compare the size evolution for all galaxies with previous JWST-based work from Varadaraj et al. (2024), Ormerod et al. (2024), Allen et al. (2025) and Yang et al. (2025).

We also measured the size of the galaxies. And since there are galaxies from very different cosmic times in our images, we are able to trace the evolution of their sizes with the age of the Universe.

disk-dominated population exhibiting larger disks by approximately 0.2 kpc, as expected. The bulge-dominated population may s... (~1 kpc) out to $z \sim 2.5$ and increase to ~3.0 kpc by $z \sim 0.6$. This suggests that the disk components of bulge-dominated galaxies begin to grow their ... at later times. Bulges, on the other hand, show little-to-no growth with redshift with the total population exhibiting bulge sizes of about 1 kpc. However, the bulge component of the bulge-dominated population displays a ... reaching $r_{bulge} \sim 1.6$ kpc. The associated 1σ dispersion is of comparable magnitude, making it difficult to draw robust conclusions.

We also investigated the size evolution of quiescent and star-forming galaxies selected using their UVJ colors in Fig. 8.

And galaxies are now 2-3 times bigger than in the early Universe!
This was already known, but thanks to our shape measurements we are able to separate the evolution of star-forming and dead galaxies.
We found that dead galaxies grew later, but faster, than star-forming galaxies!

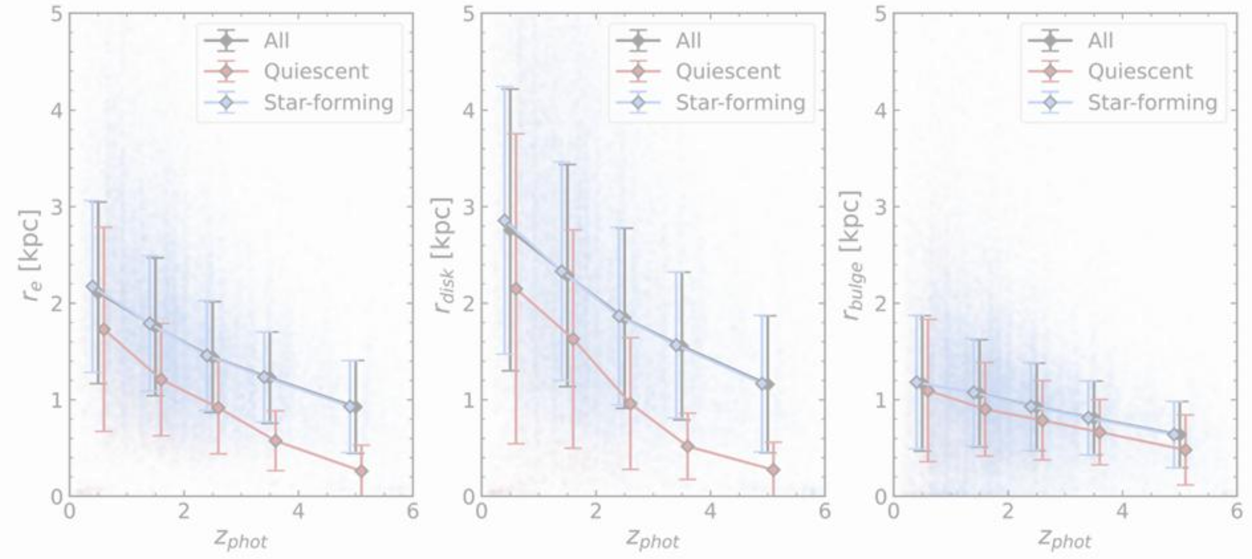

Fig. 8. Evolution of the sizes of quiescent and star forming galaxies with $\log M_\star/\mathrm{M}_\odot > 10$. The plots show the Sérsic effective radius r_e, the disk effective radius r_{disk}, and the bulge effective radius r_{bulge} as a function of $z_{\rm phot}$. Galaxies are classified as quiescent or star-forming based on their UVJ colors. The points and error bars indicate the mean and 1 σ dispersion in the corresponding $z_{\rm phot}$ bin.

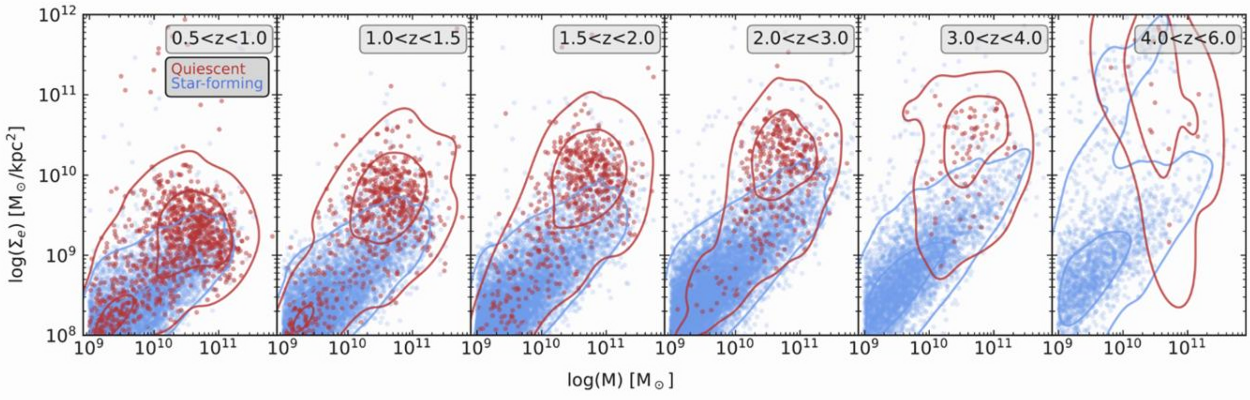

Fig. 9. Evolution of the stellar mass surface density, Σ_e. Shown are masses and redshifts from the DJA, calculated using EAZY, and effective radii, r_e, measured by SourceXtractor++ in this work. Galaxies are classified as quiescent or star-forming according to their position in the UVJ diagram. The [illegible] galaxies such that $\log M_\star/\mathrm{M}_\odot > 9$.

By combining shape, size and mass, we computed the "density" of the galaxies.

What's very interesting is that dead galaxies in the early Universe were ~10 times denser than today!

Overall, as expected, quiescent galaxies have smaller sizes than star-forming gala[illegible] with redshift, from ~0.2 kpc for the earliest quiescent galaxies at $z \sim 5$ to ~2 kpc by $z \sim 0$.[illegible] and increase in size from ~1.2 kpc to ~2.6 kpc by $z \sim 0.5$. This shows that the size growth of quiescent galaxies is steeper than that of star-forming galaxies. This size evolution is consistent with previous studies showing that both populations experience growth over time, driven by minor mergers and continuous star formation in star-forming galaxies, whereas quiescent galaxies primarily grow via dry mergers (e.g., van der Wel et al. 2014; Whitaker et al. 2017). While high-redshift quiescent galaxies are compact at formation, often referred to as "red nuggets" (e.g., Damjanov et al. 2009), Fig. 8 indicates that they continue to grow in size down to $z \sim 0.5$, a trend that can be driven by minor mergers and other accretion processes (e.g., Newman et al. 2012; Belli et al. 2015). However, part of the observed size growth of [illegible] progenitor bias – as new, larger galaxies continue to quench and enter the quiescent [illegible]rease the average size of the population, making the size evolution appear more dramatic than if individual galaxies were tracked over time (e.g., Barro et al. 2013; Carollo et al. 2013).

The disk sizes of star-forming galaxies increase from ~1.4 kpc at $z \sim 5$ to 3.4 kpc by $z \sim 0.5$, consistent with expectations from inside-out growth models, where gas accretion and star formation preferentially occur in the outskirts (e.g., Patel et al. 2012; Morishita et al. 2014; Matharu et al. 2024). The disk sizes of quiescent galaxies remain small and are similar to, or smaller than, their bulges, at least out to $z \sim 2$, where the disk size increases to about 2.6 kpc. However, the scatter is significantly higher, making it difficult to draw meaningful conclusions about the disk sizes of quiescent galaxies. The bulge sizes for both star-forming and quiescent galaxies exhibit a mild evolution with redshift. Star-forming galaxies grow by about 0.6 kpc, reaching ~1.2 kpc by $z \sim 0.5$. Quiescent galaxies are slightly more compact and, at high redshift, have bulges of about 0.4 kpc, increasing to about 1.2 kpc by $z \sim 0.6$. The persistence of small bulge sizes in both populations suggests that bulges reach their final configuration early, while the surrounding disks continue to evolve, particularly in star-forming galaxies. This is consistent with models in which early compaction events, such as mergers or disk instabilities, form a central bulge, after which the fate of the galaxy depends on the availability of fresh gas for continued star formation or quenching mechanisms (e.g., Barro et al. 2017; Tacchella et al. 2018).

4.3. Evolution of the stellar mass surface density for quiescent and star-forming galaxies

To investigate the relationship between the compactness of a galaxy and its star formation activity, we calculated the stellar mass surface density, Σ_e, which is the mass contained within the Sérsic effective radius, given by $\Sigma_e = M_\star/2\pi r_e^2$. Fig. 9 shows Σ_e as a function of stellar mass for quiescent and star-forming galaxies of $\log M_\star/M_\odot > 9$, to facilitate comparison with the existing literature, in six redshift bins at $0.5 < z < 6$. This figure demonstrates that quiescent galaxies are more compact, with higher surface mass densities than those of star-forming galaxies, and that quiescent galaxies become increasingly dense at earlier times. This finding is in good agreement with previous work, e.g., Barro et al. (2017), which shows this relation out to $z \sim 3$. Our results indicate that this relation extends out to $z \sim 5$ and that quiescent galaxies increase in compactness the earlier they form. This is consistent with the observed compactness of some of the earliest quiescent galaxies found by JWST (Carnall et al. 2023; de Graaff et al. 2025; Weibel et al. 2024; Ito et al. 2024; Wright et al. 2024).

5. Conclusions

THE END

This work presents a catalog of galaxy morphologies measured from JWST imaging of the major extragalactic surveys CEERS, GOODS, and PRIMER, processed through the DAWN JWST Archive. The catalog contains morphology information for more th[illegible] tometric redshifts extending to $z > 10$. We fitted each source with tw[illegible] model and a Bu[illegible]XTRACTOR++.

We only glanced at what this catalog of the shape of 340 000 galaxies can tell us about the evolution of galaxies and of the Universe.

To validate [illegible] our results with those from the literature obtained using independent methods and software, and we find good consistency. To demonstrate the scienti[illegible]ements in combination with the photo-z and physical parameters from the DJA EAZY catalogs. We investigate[illegible] between gala[illegible]ation activity, and redshift. We summarize our results as follows:

We confirmed a very good link between how compact a galaxy is and whether it produces stars or not.

We also measured the size evolution of these galaxies through cosmic times, and especially how their shape has varied.

– [illegible]e-dominated galaxies predominantly reside in the quiescent region, whereas [illegible] galaxies exhibit [illegible]ity in these distributions, with some populations of quiescent galaxies that are [illegible]s well as star-forming galaxies that are bulge-dominated;

– The two-component fits reveal that low B/T galaxies preferentially occupy the star-forming UVJ region, while high B/T galaxies populate the quiescent region. At $z > 3$, however, we observe a population of high B/T and bulge-dominated galaxies, consistent with a blue nugget phase;

– The Sérsic effective radius (r_e), disk effective radius (r_{disk}), and bulge effective radius (r_{bulge}) all show a decreasing trend with increasing redshift. Star-forming galaxies exhibit systematically larger sizes compared to quiescent galaxies at all redshifts, consistent with prior studies. Quiescent galaxies, while smaller than star-forming ones, show a steeper increase in their effective radius with time;

– Quiescent galaxies are significantly more compact than their star-forming counterparts, leading to high stellar mass surface densities (Σ_e). We find that Σ_e for quiescent galaxies is nearly an order of magnitude higher at $z \sim 4$ compared to $z \sim 1$, consistent with the observed compactness of some of the earliest quiescent galaxies observed by JWST.

This morphological catalog is a valuable addition to the DJA, enabling a range of in-depth studies of the morphological transformations associated with galaxy evolution.

Data availability

Our catalog is available at the CDS via anonymous ftp to [illegible]
cdsarc.cds.unistra.fr/viz-bin/cat/J/A+A/699/A343. [illegible] used to run the model fitting and the notebooks used to analyze the results are available on GitHub under the GNU GPL v3.0 li[illegible]

Our catalog is publicly available to any researchers who might be interested!

Because that's the nice thing in the scientific world: results are generally shared to make the collective human knowledge progress!

Acknowledgements. The data products presented herein were retrieved from the DA[illegible]ter (DAWN), which is funded by the Danish National Research Foundation under grant DNRF140. T[illegible]Swiss State Secretariat for Education, Research and Innovation (SERI) under contract number MB22.00072 This work has been conducted during the research internship of Aurélien Genin at the Cosmic DAWN Center, under the supervision of Marko Shuntov. This internship has also been made possible thanks to the financial support of the "Space: Science and Challenges of Space" chair at Ecole polytechnique, financed by ArianeGroup and Thales Alenia Space, as well as an Erasmus+ internship grant.

References

Allen, N., Oesch, P. A., Toft, S., et al. 2025, A&A, 698, A30
Barro, G., Faber, S. M., Pérez-González, P. G., et al. 2013, ApJ, 765, 104
Barro, G., Faber, S. M., Pérez-González, P. G., et al. 2014, ApJ, 791, 52
Barro, G., Faber, S. M., Koo, D. C., et al. 2017, ApJ, 840, 47
Belli, S., Newman, A. B., & Ellis, R. S. 2015, ApJ, 799, 206
Belli, S., Newman, A. B., & Ellis, R. S. 2019, ApJ, 874, 17
Berman, E. M., McCleary, J. E., Koekemoer, A. M., et al. 2024, AJ, 168, 174
Bertin, E. 2011, in Astronomical Data Analysis Software and Systems XX, eds. I. N. Evans, A. Accomazzi, D. J. Mink, & A. H. Rots, Astronomical Society of the Pacific Conference Series, 442, 435
Bertin, E., & Arnouts, S. 1996, A&ASS, 117, 393
Bertin, E., Schefer, M., Apostolakos, N., et al. 2020, in Astronomical Data Analysis Software and Systems XXIX, eds. R. Pizzo, E. R. Deul, J. D. Mol, J. de Plaa, & H. Verkouter, Astronomical Society of the Pacific Conference Series, 527, 461
Brammer, G., van Dokkum, P. V., & Coppi, P. 2008, ApJ, 686, 1503
Carnall, A. C., McLure, R. J., Dunlop, J. S., et al. 2023, Nature, 619, 716
Carollo, C. M., Bschorr, T. J., Renzini, A., et al. 2013, ApJ, 773, 112
Conselice, C. J. 2003, ApJS, 147, 1
Conselice, C. J. 2014, ARA&A, 52, 291
Cortese, L., Catinella, B., & Smith, R. 2021, PASA, 38, e035
Daddi, E., Renzini, A., Pirzkal, N., et al. 2005, ApJ, 626, 680

Damjanov, I., McCarthy, P. J., Abraham, R. G., et al. 2009, ApJ, 695, 101
de Graaff, A., Setton, D. J., Brammer, G., et al. 2025, Nat. Astron., 9, 280
de Vaucouleurs, G. 1959, Handb. Phys., 53, 275
Dekel, A., & Burkert, A. 2014, MNRAS, 438, 1870
D'Eugenio, F., Pérez-González, P. G., Maiolino, R., et al. 2024, Nat. Astron., 8, 1443
Donnan, C. T., McLure, R. J., Dunlop, J. S., et al. 2024, MNRAS, 533, 3222
Eisenstein, D. J., Willott, C., Alberts, S., et al. 2023, arXiv e-prints, [arXiv:2306.02465]
Ester, M., Kriegel, H.-P., Sander, J., & Xu, X. 1996, in Second International Conference on Knowledge Discovery and Data Mining (KDD'96), Proceedings of a conference held August 2–4, 226
Fall, S. M., & Efstathiou, G. 1980, MNRAS, 193, 189
Finkelstein, S. L., Bagley, M. B., Ferguson, H. C., et al. 2023, ApJ, 946, L13
Fischler, M., & Bolles, R. 1981, Commun. ACM, 24, 381
Grogin, N. A., Kocevski, D. D., Faber, S. M., et al. 2011, ApJS, 197, 35
Gunn, J. E., & Gott, III, J. R. 1972, ApJ, 176, 1
Heintz, K. E., Brammer, G. B., Watson, D., et al. 2025, A&A, 69[illegible]
Hubble, E. P. 1936, Realm of the Nebulae (New Haven: Yale University Press)
Ito, K., Valentino, F., Brammer, G., et al. 2024, ApJ, [illegible], 192
Kawinwanichakij, L., Silverman, J. D., D[illegible], et al. 2021, ApJ, [illegible]21, 38
Koekemoer, A. M., Aussel, H., Calzetti, D., et al. 2007, ApJS, 172, 196
Koekemoer, A. M., Faber, S. M., Ferguson, Henry C., et al. 2011, ApJS, 197, 36
Kümmel, M., Bertin, E., Schefer, M., et al. 2020, in Astronomical Data Analysis Software and Systems XXIX, eds. R. Pizzo, E. R. Deul, J. D. Mol, J. de Plaa, & H. Verkouter, Astronomical Society of the Pacific Conference Series, 527, 29
Larson, R. B., Tinsley, B. M., & Caldwell, C. N. 1980, ApJ, 237, 692
Leauthaud, A., Massey, R., Kneib, J.-P., et al. 2007, ApJS, 172, 219
Lintott, C. J., Schawinski, K., Slosar, A., et al. 2008, MNRAS, 389, 1179
Lotz, J. M., Primack, J., & Madau, P. 2004, AJ, 128, 163
Matharu, J., Nelson, E. J., Brammer, G., et al. 2024, A&A, 690, A64
Mo, H. J., Mao, S., & White, S. D. M. 1998, MNRAS, 295, 319
Moore, B., Katz, N., Lake, G., Dressler, A., & Oemler, A. 1996, Nature, 379, 613
Moore, B., Lake, G., & Katz, N. 1998, ApJ, 495, 139
Moran, S. M., Ellis, R. S., Treu, T., et al. 2007, ApJ, 671, 1503
Morishita, T., Ichikawa, T., & Kajisawa, M. 2014, ApJ, 785, 18
Moutard, T., Sawicki, M., Arnouts, S., et al. 2018, MNRAS, 479, 2147
Newman, A. B., Ellis, R. S., Bundy, K., & Treu, T. 2012, ApJ, 746, 162
Oke, J. B. 1974, ApJS, 27, 21
Omand, C. M. B., Balogh, M. L., & Poggianti, B. M. 2014, MNRAS, 440, 843
Ormerod, K., Conselice, C. J., Adams, N. J., et al. 2024, MNRAS, 527, 6110
Patel, S. G., Holden, B. P., Kelson, D. D., et al. 2012, ApJ, 748, L27
Peng, Y., Lilly, S. J., Kovac, K., et al. 2010, ApJ, 721, 193
Planck Collaboration VI. 2020, A&A, 641, A6
Quilley, L., & de Lapparent, V. 2022, A&A, 666, A170
Rieke, M., Kelly, D., & Horner, S. 2005, in SPIE Optics + Photonics, 5904
Rix, H.-W., Barden, M., Beckwith, S. V. W., et al. 200[illegible], ApJS, 152, 163
Robitaille, T. 2018, https://doi.org/10.5281/zenodo.1162674
Schawinski, K., Urry, C. M., Simmons, B. D., et al. 2014, MNRAS, 440, 889
Schreiber, C., Elbaz, D., Pannella, M., et al. 2016, A&A, 589, A35
Sérsic, J. L. 1963, Bol. Asoc. Argentina Astron. Plata Argentina, 6, 41
Shen, S., Mo, H. J., White, S. D. M., et al. 2003, MNRAS, 343, 978
Shibuya, T., Ouchi, M., & Harikane, Y. 2015, ApJS, 219, 15
Somerville, R. S., Behroozi, P., Pandya, V., et al. 2018, MNRAS, 473, 2714
Tacchella, S., Carollo, C. M., Renzini, A., et al. 2015, Science, 348, 314
Tacchella, S., Dekel, A., Carollo, C. M., et al. 2016, MNRAS, 458, 242
Tacchella, S., Carollo, C. M., Förster Schreiber, N. M., et al. 2018, ApJ, 859, 56
Toft, S., Zabl, J., Richard, J., et al. 2017, Nature, 546, 510
Trujillo, I., Conselice, C. J., Bundy, K., et al. 2007, MNRAS, 382, 109
Valentino, F., Brammer, G., Gould, K. M. L., et al. 2023, ApJ, 947, 20
van der Wel, A., Bell, E. F., Häussler, B., et al. 2012, ApJS, 203, 24
van der Wel, A., Franx, M., van Dokkum, P. G., et al. 2014, ApJ, 788, 28
van Dokkum, P. G., Nelson, E. J., Franx, M., et al. 2015, ApJ, 813, 23
Varadaraj, R. G., Bowler, R. A. A., Jarvis, M. J., et al. 2024, MNRAS, 533, 3724
Weibel, A., Oesch, P. A., Barrufet, L., et al. 2024, MNRAS, 533, 1808
Whitaker, K. E., Bezanson, R., van Dokkum, P. G., et al. 2017, ApJ, 838, 19
Williams, R. J., Quadri, R. F., Franx, M., van Dokkum, P., & Labbé, I. 2009, ApJ, 691, 1879
Wright, L., Whitaker, K. E., Weaver, J. R., et al. 2024, ApJ, 964, L10
Yang, L., Kartaltepe, J. S., Franco, M., et al. 2025, COSMOS-Web: Unraveling the Evolution of Galaxy Size and Related Properties at 2 < z < 10
York, D. G., Adelman, J., Anderson, John E., J., et al. 2000, AJ, 120, 1579
Zolotov, A., Dekel, A., Mandelker, N., et al. 2015, MNRAS, 450, 2327

And since we've quoted the work of a lot of different persons,
we have to cite them properly.

Thank you for reading this, and congratulations for reaching the end ! I hope you learned new stuff about the life of galaxies, and that my attempt to make this paper understandable was clear enough

Aurélien Genin
https://astroaure.github.io

I had the idea to make this simplified version of my paper from Claire Lamman who does a wonderful job! See clairelamman.com for more.
And as her, I've used the XKCD font for it: https://github.com/ipython/xkcd-font
The JWST skecth at the beginning comes from MAST.